Photothermal Contribution to Enhanced Photocatalytic Performance of Graphene-Based Nanocomposites

Zhixing Gan,[†] Xinglong Wu,[†,*] Ming Meng,[†] Xiaobin Zhu,[†] Lun Yang,[†] and Paul K. Chu[‡]

[†]Key Laboratory of Modern Acoustics, MOE, Institute of Acoustics, National Laboratory of Solid State Microstructures and Department of Physics, Nanjing University, Nanjing, 210093 P. R. China and [‡]Department of Physics and Materials Science, City University of Hong Kong, Tat Chee Avenue, Kowloon, Hong Kong, China

ABSTRACT Photocatalysts possessing high efficiency in degrading aquatic organic pollutants are highly desirable. Although graphene-based nanocomposites exhibit excellent photocatalytic properties, the role of graphene has been largely underestimated. Herein, the photothermal effect of graphene-based nanocomposites is demonstrated to play an important role in the enhanced photocatalytic performance, which has not been considered previously. In our study on degradation of organic pollutants (methylene blue), the contribution of the photothermal effect caused by a nanocomposite consisting of P25 and reduced graphene oxide can be as high as ~38% in addition to trapping and shuttling photogenerated electrons and increasing both light absorption and pollutant adsorptivity. The result reveals that the photothermal characteristic of graphene-based nanocomposite is vital to photocatalysis. It implies that designing graphene-based nanocomposites with the improved photothermal performance is a promising strategy to acquire highly efficient photocatalytic activity.

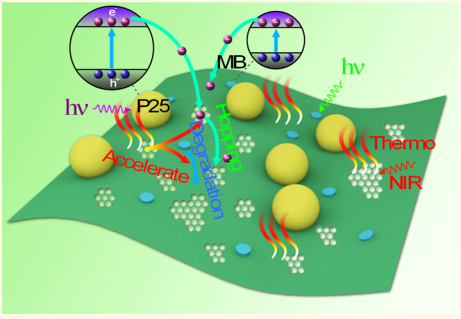

KEYWORDS: graphene · P25 · photocatalyst · photothermal effect

The reduction of graphene oxide (GO) is a popular and efficient way to synthesize graphene,[1,2] and the reduced graphene oxide (rGO) has many potential applications.[3−6] For example, nanocomposites composed of rGO exhibit excellent photocatalytic properties such as degradation of dyes, reduction of CO_2, and water splitting.[7−20] Although the role played by rGO in photocatalytic performance has been extensively investigated,[13−20] the complexity of the rGO structure including sp^2 and sp^3 hybridized carbon atoms, various functional groups, and defects makes it difficult to well understand some electrical and optical properties,[3,21−23] and thus some new explorations in developing highly efficient photocatalysts have been hampered. Lee *et al.* suggested that more sunlight in the visible range was harnessed due to the upconversion introduced by graphene thus leading to enhanced photocatalytic degradation.[20] However, our recent work confirmed that the so-called upconversion photoluminescence (PL) from rGO excited by noncoherent light was artificial and only photons of a pulsed laser could be up-converted;[24] hence, the enhanced photocatalytic degradation cannot be attributed to the upconversion PL. The three common and important functions of rGO in the photocatalysis of rGO−semiconductor nanoparticle composites, widely discussed so far, are trapping and shuttling of photogenerated electrons, increasing adsorption of pollutants, and extending light absorption,[13−18] but these cannot fully explain the photocatalytic activity. We know that rGO has a strong photothermal effect (PTE) which may also be a key factor in the photocatalytic performance but up until now it has completely been ignored.

In PTE, which has been employed to kill cancerous cells,[25−28] photoexcitation creates thermal energy (heat). Traditional photothermal materials are mainly based on gold nanostructures,[25] but recently, biocompatible rGO which has excellent photothermal properties has been increasingly used in cancer therapy.[27,28] In the photodegradation of pollutants, although the temperature of the reaction vessel is kept approximately constant, rGO still generates thermal energy continuously under

* Address correspondance to hkxlwu@nju.edu.cn.

Received for review June 15, 2014 and accepted August 25, 2014.

Published online August 25, 2014
10.1021/nn503249c

irradiation thus affecting the transportation of the photogenerated carriers on the rGO sheet. This will significantly improve the photocatalytic activity. In this work, the photodegradation of methylene blue (MB) by the P25(TiO_2)-rGO nanocomposites is studied, and the contribution of PTE, which is induced by near-infrared (NIR) light, is evaluated to be as high as ~38% in the whole degradation action of organic pollutants. This suggests that PTE plays a crucial role in the photocatalytic performance of rGO-based nanocomposites. It is well-known that NIR light is an important part of sunlight, but it is directly absorbed only with difficulty by regular semiconductor. Thus, our work shows an effective route to improve utilization efficiency of solar energy through PTE.

RESULTS

The P25−rGO nanocomposites were fabricated using established procedures.[17,18] The GO was synthesized by the Hummers method,[29] and the structural characterization is described elsewhere.[24,30] A one-step hydrothermal method was employed to reduce GO and combine with P25. Figure 1a shows the transmission electron microscopy (TEM) image of a P25−rGO nanocomposite comprising 5 wt % rGO [P25−rGO (5 wt %)]. The P25 nanoparticles (black arrow) with a diameter of about 20 nm are attached to the rGO sheet (white arrow). (More structural characterization of the P25−rGO nanocomposites by X-ray diffraction (XRD), Fourier transform infrared (FTIR), and diffusion reflectance absorption spectra is described in the Supporting Information, Figure S1.) The structural characterization confirms the reduction of GO and combination of P25 with rGO. The results also show that the P25−rGO nanocomposites are similar to those reported previously,[17,18] and so a valid comparison can be made.

The P25 and P25−rGO powders were used as photocatalysts to degrade MB. First, the powders were added to the MB solution separately and stirred overnight to reach adsorption equilibrium. Figure 1b shows the initial and remaining concentration fractions of MB after the adsorption equilibrium. More dye molecules are observed to adsorb onto the surface of P25−rGO validating its higher absorption efficiency which is crucial to the photocatalytic performance of rGO-based materials.[17,18]

Degradation of MB by P25 and P25−rGO is performed on the experimental setup illustrated in Supporting Information, Figure S2a. The vessel was immersed in a sink in which the water is kept at a nearly constant temperature of ca. 25 °C. A 200 W xenon lamp was used as the irradiation source, and a filter was used to select the wavelength range. By using a 720 nm short-pass (SP) filter, nearly all the light in the NIR region is removed and visible light (Vis) is also partially attenuated. The irradiation condition is labeled

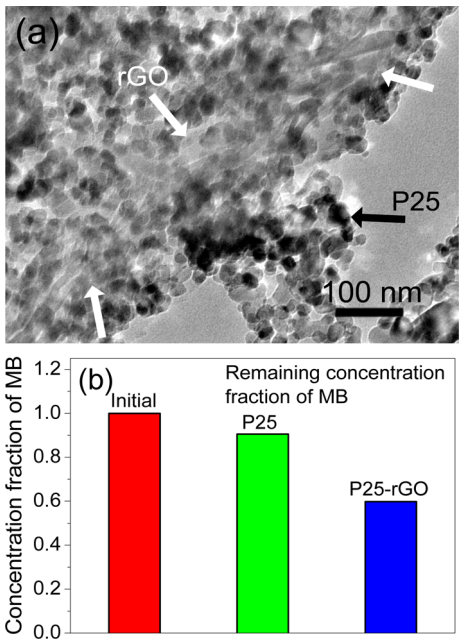

Figure 1. (a) P25−rGO (5 wt %) with the white and black arrows indicating the rGO sheets and P25 nanoparticles, respectively. (b) Remaining MB concentrations in the initial, P25, and P25−rGO solutions, respectively, after reaching adsorption equilibrium by stirring overnight in darkness.

as ultraviolet (UV)+Vis. The transmission spectrum of the SP filter is shown in the Supporting Information, Figure S3. In the second scenario, by using a 720 nm long-pass (LP) filter, only NIR light is allowed to pass, and this condition is designated as NIR. The average results of three independent photodegradation experiments are shown in Figure 2a. Curve 1 does not show obvious MB degradation by P25−rGO under irradiation of NIR, indicating that no chemically reactive electrons are generated by the NIR light. Curve 1 also confirms that the adsorption equilibrium has been reached before photodegradation and self-degradation of MB is negligible. Curves 2 and 3 illustrate MB degradation by P25 and P25−rGO under UV+Vis light, respectively, and curves 4 and 5 correspond to the degradation of MB by P25 and P25−rGO when illuminated by a xenon lamp covering the entire wavelength range. Comparison between curves 4 and 5 shows that P25−rGO has higher catalytic activity and by comparing curves 2 and 4 or 3 and 5, the degradation rate is reduced in the presence of the SP filter. It is noted that the gap between curves 3 and 5 is much larger than that between curves 2 and 4.

The temperature rise detected from the P25 and P25−rGO suspensions under NIR light exposure is depicted in Supporting Information, Figure S4. The experimental conditions including the sample concentration, stirring time, irradiation power, and time are the same as those in the previous photocatalytic experiments but no external cooling water is used. The temperature variations measured from pure water

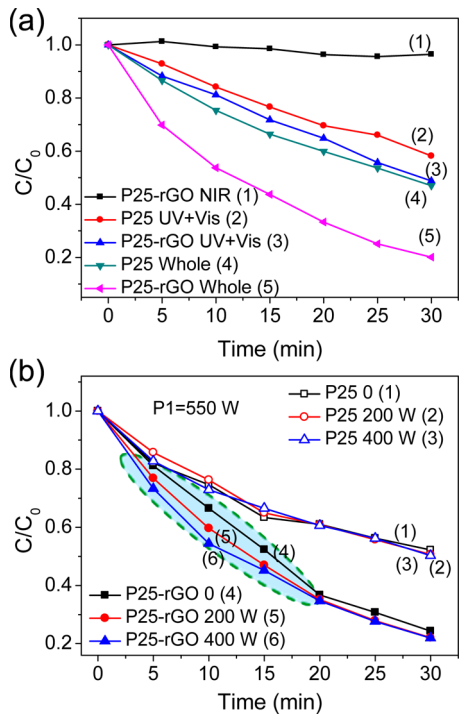

Figure 2. (a) Photocatalytic degradation of MB on P25 or P25−rGO. (b) Photocatalytic degradation of MB on P25 and P25−rGO illuminated by two lamps. Lamp 1 with a fixed power provides light in the whole wavelength range and the power of lamp 2 (NIR) is varied (inset).

and P25 suspension are almost the same, whereas the temperature increase of the P25−rGO suspension is faster due to the PTE of rGO. An additional temperature increment of 2.2 °C is observed within an irradiation time of 30 min owing to the introduction of the rGO compared to the situation of pure water and P25 suspension. More than 924 J is calculated to be generated by the rGO. Concerning the degradation of MB, the following situation possibly occurs. As shown in Supporting Information, Figure S3, when a light beam passes through the SP filter, not only is the NIR portion cut off, but also the visible light in the range of 600−720 nm is attenuated partially. The gap between curves 2 and 4 arises from reduction in the visible light caused by the SP filter, and the decreased NIR light can be ignored. With regard to curves 3 and 5 of P25−rGO, the PTE of rGO under NIR exposure is also weakened by the filter in addition to light attenuation in the range of 600−720 nm. However, the PTE is positive, and the SP filter results in a bigger gap between curves 3 and 5.

To verify the above hypothesis, photodegradation experiments are performed by irradiation with two lamps. In the experimental setup shown in the Supporting Information, Figure S2b, a 550 W xenon lamp (lamp 1) without a filter is placed on the side to provide UV+Vis+NIR irradiation with a fixed power density. Alternatively, lamp 2 exports NIR light. The power of lamp 2 can be adjusted (0, 100, 200 W) to study the impact of NIR on the photocatalytic process. As shown in Figure 2b (curves 1−3), degradation of MB by P25 is independent of the power of lamp 2. In other words, NIR irradiation does not affect the chemical reaction. Curves 4−6 in Figure 2b show that the photocatalytic performance of P25−rGO improves with the power of lamp 2. The difference between curves 4−6 is obvious during the initial irradiation duration of 20 min (gray region). After 20 min of irradiation, ~70% of the MB is degraded, and the residual amount of MB is largely reduced. This implies that the amount of MB captured by P25−rGO is also obviously reduced, which makes the degradation rate independent of the NIR irradiation, and the difference between curves 4−6 becomes inconspicuous. Hence, NIR irradiation plays an important but auxiliary role in the enhanced photocatalytic performance of P25−rGO, since the NIR light alone cannot produce photodegradation (curve 1 in Figure 2a).

The auxiliary function of NIR in the enhancement caused by rGO is studied. However, the change in the MB concentration during photodegradation is nonlinear and degradation slows gradually. The total degradation rate is defined as $R_D = \Delta m$/time. Since the time (30 min) is fixed in the experiments, the differences in Δm are compared. Δm represents the degraded amount of MB and contains two parts, variation in the solution (Δm_{so}) which can be obtained from Figure 2a and mass variation of MB on the surface of the photocatalysts (Δm_{su}), where $\Delta m_{su} = m_{ad} - m_{re}$; m_{ad} represents the mass of MB adsorbed by the photocatalysts after reaching adsorption equilibrium shown in Figure 1b, and m_{re} is the mass of residual MB on the surface of the photocatalysts after photodegradation experiments. The values of m_{re} are estimated from the TGA results, and the details are presented in the Supporting Information, Figure S5. The calculation of MB degradation by P25 irradiated by the xenon lamp without NIR light (curve 2 in Figure 2a) is shown here as an example: $\Delta m_{so\text{-}2} = (1 - 58.2\%) \times 90.5\% \times 5$ ppm $\times$ 200 mL = 378.29 μg, and $m_{ad\text{-}2} = (1-90.5\%) \times 5$ ppm $\times$ 200 mL = 95 μg. Hence, $\Delta m_2 = \Delta m_{so\text{-}2} + \Delta m_{su\text{-}2} = \Delta m_{so\text{-}2} + m_{ad\text{-}2} - m_{re\text{-}2} = 378.29 + 95 - 33.2 = 440.09$ μg. Similarly, Δm_3 = 608.55 μg, Δm_4 = 524.85 μg, and Δm_5 = 846.60 μg are obtained. The proportion of the auxiliary function of NIR light in the enhancement caused by rGO is calculated as follows: $P = (\delta_c - f \times \delta_b)/\delta_a$, where $\delta_a = \Delta m_5 - \Delta m_4$ represents the enhancement between P25−rGO and P25, $\delta_b = \Delta m_4 - \Delta m_2$ reflects the influence caused by the SP filter for P25. Figure 2b confirms that NIR irradiation does not affect the degradation by P25 (more discussion is presented in Supporting Information, Figure S6), and so δ_b mainly reflects the light attenuation in the visible part caused by the SP filter. $\delta_c = \Delta m_5 - \Delta m_3$ is the difference caused by the SP filter for P25−rGO. δ_c contains two parts, light attenuations in NIR and visible light. $f = \Delta m_3/\Delta m_2$ is the MB degradation rate ratio

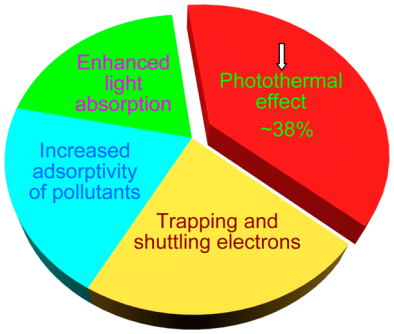

Figure 3. Contribution of graphene in the enhanced photocatalytic activity. There are four main factors for the enhanced photocatalytic performance introduced by rGO. In our study of the degradation of MB, the contribution of PTE caused by P25−rGO can be as high as ~38%.

between P25−rGO and P25 under UV+Vis exposure. Thus, P = 37.6% is obtained. Here, we should point out that MB can absorb photons at about 650 nm (the sensitization of MB) (the absorption spectrum of MB solution is shown in Supporting Information, Figure S7). This sensitization effect has been included in δ_b which has been subtracted in our above calculation. To further rule out the influence of the sensitization effect, we have also studied the photocatalytic activities of P25−rGO in 2-hydroxy terephthalic acid by calculating the amount of OH radicals[31] and estimated the photothermal contribution (Supporting Information, Figure S8). A ~34% photothermal contribution is obtained after a careful calculation.[31] This indicates that the photothermal effect is really dominant.

As shown in Figure 3, the increasing adsorption of pollutants, extended light absorption range, and charge transportation and separation are indeed responsible for the enhanced photocatalytic performance.[17,18] However, besides these factors, our experiments clearly reveal that the auxiliary function of NIR light is also crucial to the photocatalytic performance and this has not been understood in the literature. Here we would like to mention that we have also fabricated the P25−rGO nanocomposites with different wt % of rGO and carried out the corresponding photodegradation testing (Supporting Information, Figure S9). Compared to the case from P25, the enhanced photodegradation rates over P25−rGO (1 wt %) and P25−rGO (10 wt %) are not big enough, while the photodegradation over P25−rGO (5 wt %) is the most efficient. This result is well consistent with the previous report by Zhang et al.[18] Since the photothermal contribution is just one part of the enhancement, we only used the P25−rGO (5 wt %) to estimate the photothermal contribution in this work.

As shown in Supporting Information, Figure S4, PTE is important during the NIR light irradiation of rGO. Although the additional temperature increment caused by rGO is just 2.2 °C, the heat energy, which is initially localized around the rGO/TiO_2 composite, is as large as 924 J by our calculation. If considering the relatively small amount of rGO (about 1.25 mg), the heat generated by a single rGO sheet will increase the local temperature up 36 °C after 60 min of irradiation, which is a substantial amount much higher than the external cooling water especially at the early stage (Supporting Information, Figure S6). Even though the degradation of MB is performed at a nearly constant external temperature, such local thermal energy by the rGO still has a significant influence on the chemical reaction. Since NIR light cannot excite either P25 or dyes, almost no electrons can be generated, and the dyes are thus not degraded by NIR light alone. However, in conjunction with UV+Vis light, the heat generated by NIR light can accelerate the degradation process remarkably. Conversely, the photothermal effect of rGO under UV and visible irradiation is not noticeable (Supporting Information, Figure S4).

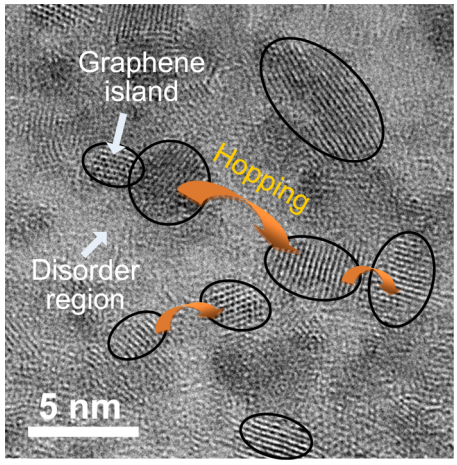

Figure 4. HRTEM image of a rGO sheet. The rGO sheet contains graphene islands (black circles) separated by disordered regions.

DISCUSSION

At present, very little is known about the inherent mechanism of PTE in rGO, although the phenomenon is utilized in cancer therapy.[26−28] Similar to noble metal nanostructures, PTE of rGO under NIR irradiation is mainly caused by surface plasmon resonance (SPR). The lattice acquires energy from the incident electromagnetic wave and vibrates dramatically. Plasmon describes the collective oscillation of electrons and as reported previously, electrons in graphene are two-dimensional (2D) massless electrons (so-called Dirac Fermions).[32,33] The light and plasmon coupling from Dirac Fermions in graphene is remarkably strong and the integrated oscillator strength of graphene plasmon is an order of magnitude larger than that observed from conventional 2D electron systems.[32] Figure 4 shows the high resolution TEM (HR-TEM) image of a single rGO sheet. The rGO sheet contains graphene islands separated by disordered regions consistent

with previous reports.[22,34] The electrons in the graphene islands behave like Dirac Fermions and the plasmon of rGO produces an ensemble effect of collective oscillation of electrons confined in various graphene islands with different sizes. For plasmon of graphene with a limited lateral size (graphene nanoribbons and nanodisks), the scaling of the plasmon frequency ω_P follows the following relationship: $\omega_P \propto (E_f/D)^{1/2}$, where D is the lateral size and E_f is the Fermi level that can be deduced by $n = (|E|_f/\hbar v_f)^2/\pi$, where $v_f \approx 10^6$ m/s is the Fermi velocity and n is the carrier concentration.[32,33] Therefore, the plasmon frequency is determined by the graphene island size and carrier concentration. Assuming that the carrier concentration is on the order of 10^{12} cm^{-2} and the island size is about 1−10 nm, the SPR wavelength is estimated to be about 1000 nm.[32] Since the plasmon resonance of Dirac Fermions has remarkably large oscillator strengths, room-temperature optical absorption peaks can be observed.[31] The extinction spectrum of the rGO suspension is shown in Supporting Information, Figure S10 in which several notable absorption peaks in the range of 700−1300 nm can be observed. They originate from plasmon oscillation of the graphene islands confined in the rGO sheets with different sizes.

The role played by PTE in enhanced photodegradation of MB is described in the following. The crucial role of the photocatalytic process is the separation and transfer of photogenerated charge carriers. First, the temperature variation may affect the carrier mobility in the rGO sheet. Generally speaking, massless Dirac Fermions of the ideal graphene sheet have ultrahigh mobility, but for chemically derived rGO sheets, the carrier mobility is lower than that of pristine graphene by about 2−3 orders of magnitude.[22] The chemically derived rGO sheet constitutes a structurally and electronically inhomogeneous system. As shown in Figure 4, a single rGO sheet contains both graphene islands and disordered regions. The carriers in the graphene islands act like delocalized state carriers, but for these disordered regions with localized states, conduction is mainly realized by hopping.[22,34] The conductance of a rGO sheet can be described by the two-dimensional variable range hopping (2D VRH) mechanism with the following relationship: $G(T) = G_1 \exp(-B/T^{1/3})$. The hopping parameter B depends on the density of states $N(E_f)$ near the Fermi level and localization length L_l of the electronic wave functions. In 2D VRH, the dependence is given by $B = (3/kN(E_f)L_l^2)^{1/3}$, where k is Boltzmann's constant.[22,34] Hence, a higher carrier mobility is expected at higher temperature.[22,34] A higher carrier mobility of rGO sheets raised by the PTE can be the most dominant factor that causes the enhanced photocatalytic performance of P25−rGO nanocomposites.

Second, the enhanced photocatalytic performance is possibly due to the variation of the photoexcited

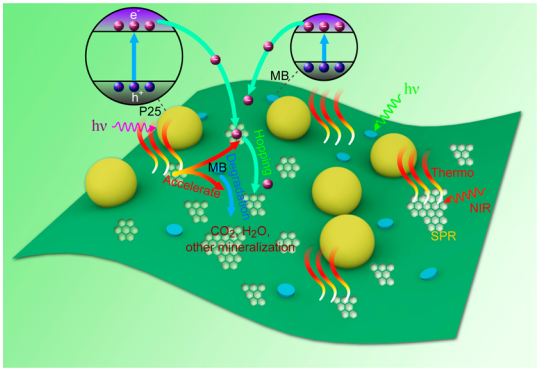

Figure 5. Mechanism of MB degradation over P25−rGO. Surface plasmon resonance (SPR) under NIR irradiation leads to PTE of rGO. Thermal energy promotes carrier mobility on rGO sheets and thus results in the improved photodegradation activity.

efficiency in P25 during the temperature rise. The carrier-photogenerated rate G under irradiation with a power density of J is $G = \alpha(\hbar\omega)J/\omega$, where $\alpha(\hbar\omega)$ is the optical absorption coefficient. For P25 containing rutile and anatase TiO_2, both direct and indirect transitions coexist. Regarding direct transition, only photons with energy $\hbar\omega \geq E_g$ can be absorbed. The absorption coefficient is $\alpha(\hbar\omega) = A(\hbar\omega - E_g)^{1/2}$, which is independent of the temperature. For indirect transition, a phonon with energy of E_{ph} is involved and $\alpha'(\hbar\omega)$ is positively related to the temperature. However, usually $\alpha'(\hbar\omega) \ll \alpha(\hbar\omega)$ and the overall optical transition process of P25 is nearly independent of temperature.

Finally, the hot carrier relaxation in rGO during the temperature variation is discussed. The relaxation of photogenerated carriers usually consists of several processes such as carrier−carrier interaction, carrier−phonon scattering (mainly optical phonon emission), Auger recombination, and carrier trapping.[35,36] Ruzicka *et al.* have revealed that the relaxation of a hot carrier in rGO is independent of the temperature,[35] and the carriers have a hot distribution immediately after photoexcitation. Consequently energy relaxation is dominated by carrier-phonon scattering. A large number of optical phonons are emitted giving rise to significant deviation of the phonon distribution in the excitation spot away from the equilibrium distribution dictated by the sample temperature. Regarding the photothermal process, it is a collective electronic effect so that the lattice temperature reaches equilibrium rapidly. Therefore, the hot carriers experience a much higher lattice temperature than the temperature of other parts of the sample, and the finite temperature variation has no influence on the carrier dynamics.

On the basis of the above results and discussions, we can explain the high photocatalytic performance of P25−rGO as follows (Figure 5). Under solar light or xenon lamp illumination, the UV part excites P25 while both UV and visible light excite MB. Both processes generate electron−hole pairs, and the separation of

electrons and holes will be favored due to the shuttling of rGO sheets. NIR irradiation heats up the rGO sheets because of PTE. This causes the electrons to obtain more energy and move faster on the hot rGO sheets. As a result, PTE promotes the degradation of pollutants on the nanocomposites. It is believed that similar effects also occur in other graphene-based nanocomposites and are important to photocatalysis in environment and energy applications including degradation of dyes, reduction of CO_2, and water splitting. Recently, enhanced photothermal effects of graphene-based nanocomposites have been reported.[37,38] Our result implies that such nanocomposites with improved photothermal performance have more favorable applications.

CONCLUSION

For graphene-based nanocomposites, graphene was mainly considered to have three common and important functions, trapping and shuttling photogenerated electrons and increasing both light absorption and pollutant adsorptivity. In this work, we reveal that not only does PTE exist but also its contribution in P25−rGO nanocomposites can be as high as ~38% in the entire degradation action of organic pollutants. The result demonstrates that the photothermal characteristic of graphene-based nanocomposites is vital to photocatalysis, and designing nanocomposites with the improved photothermal performance is a promising strategy to acquire highly efficient photocatalytic activity.

METHODS

Sample Preparation. P25 (20% rutile and 80% anatase TiO_2) was purchased from Degussa (Germany), and GO was synthesized by the Hummers method. The P25−5% rGO was fabricated by a hydrothermal technique as follows: 31.5 mg of GO and 0.6 g of P25 were dissolved in a solution of deionized water (60 mL) and ethanol (30 mL), stirred, and treated ultrasonically. The suspension was placed in a 100 mL Teflon-sealed autoclave and kept at 120 °C for 24 h. The products were washed by deionized water and ethanol several times and dried at 60 °C. Here we stress that if there is no special description, the "P25−rGO" represents the "P25−rGO (5 wt %)".

Characterization. The FTIR spectra were recorded on the NEXUS 870 spectrometer, and X-ray diffraction (XRD) was performed on the ARL X′ TRA X-ray diffractometer. TEM was conducted on P25−rGO on the JEOL-2100F electron microscope and the HR-TEM images of the rGO were acquired on an aberration corrected TEM (FEI Titan 80-300). The diffusion reflectance absorption spectra were obtained on a Shimadzu UV-2550 spectrometer with an integrating sphere attachment.

Photocatalytic Experiments. In brief, 25 mg of the catalyst (P25 or P25−rGO) were added to 100 mL of 5 ppm MB. The suspension was stirred overnight to reach equilibrium prior to light exposure. Two xenon lamps were used. The reaction vessel was put in a sink in which the externally circulated water was kept at an approximately constant temperature at 25 °C. The concentration of MB in each stage was monitored by a UV−vis−NIR spectrophotometer (UV 3600, Shimadzu). To estimate the heat generated by rGO, the experimental conditions including the sample concentration, stirring time, irradiation power, and time were kept the same, except that the vessel was placed in ambient atmosphere. The temperature was recorded by a K-type thermocouple (resolution, 0.1 °C).

Conflict of Interest: The authors declare no competing financial interest.

Supporting Information Available: More structural and spectral characterizations of P25−rGO, schematic illustration of the experimental setup, temperature variation of the photocatalysts under NIR light irradiation, TGA results, absorption spectrum of MB solution, photocatalytic activities determined by the PL spectra, photocatalytic degradation of MB over P25−rGO (1 wt %) and P25−rGO (10 wt %), and extinction spectrum. This material is available free of charge *via* the Internet at http://pubs.acs.org.

Acknowledgment. Z. X. Gan thanks X. Y. Wang from Department of Physics, Nanjing University, for helpful discussion. This work was supported by grants from the National Basic Research Programs of China (Nos. 2011CB922102, 2014CB339800, and 2013CB932901) and National Natural Science Foundation (Nos. 21203098 and 11374141). Partial support was provided by the Guangdong-Hong Kong Technology Cooperation Funding Scheme (TCFS), GHP/015/12SZ.

REFERENCES AND NOTES

1. Park, S. J.; Ruoff, R. S. Chemical Methods for the Production of Graphenes. *Nat. Nanotechnol.* **2009**, *4*, 217–224.
2. Stankovich, S.; Dikin, D. A.; Dommett, G. H. B.; Kohlhaas, K. M.; Zimney, E. J.; Stach, E. A.; Piner, R. D.; Nguyen, S. T.; Ruoff, R.; Graphene-Based, S. Composite Materials. *Nature* **2006**, *442*, 282–286.
3. Loh, K. P.; Bao, Q. L.; Eda, G.; Chhowalla, M. Graphene Oxide as a Chemically Tunable Platform for Optical Applications. *Nat. Chem.* **2010**, *2*, 1015–1024.
4. Zhu, Y. W.; Murali, S.; Cai, W. W.; Li, X. S.; Suk, J. W.; Potts, J. R.; Ruoff, R. S. Graphene and Graphene Oxide: Synthesis, Properties, and Applications. *Adv. Mater.* **2010**, *22*, 3906–3924.
5. Wei, Z. Q.; Wang, D. B.; Kim, S.; Kim, S. Y.; Hu, Y. K.; Yakes, M. K.; Laracuente, A. R.; Dai, Z. T.; Marder, S. R.; Berger, C.; *et al*. Nanoscale Tunable Reduction of Graphene Oxide for Graphene Electronics. *Science* **2010**, *328*, 1373–1376.
6. Liang, Y. Y.; Li, Y. G.; Wang, H. L.; Zhou, J. G.; Wang, J.; Regier, T.; Dai, H. J. Co_3O_4 Nanocrystals on Graphene as a Synergistic Catalyst for Oxygen Reduction Reaction. *Nat. Mater.* **2011**, *10*, 780–786.
7. Xiang, Q. J.; Yu, J. G.; Jaronie, M. Graphene-Based Semiconductor Photocatalysts. *Chem. Soc. Rev.* **2012**, *41*, 782–796.
8. Maitra, U.; Gupta, U.; De, M.; Datta, R.; Govindaraj, A.; Rao, C. N. R. Highly Effective Visible-Light-Induced H_2 Generation by Single-Layer 1T-MoS_2 and a Nanocomposite of Few-Layer 2H-MoS_2 with Heavily Nitrogenated Graphene. *Angew. Chem., Int. Ed.* **2013**, *52*, 13057–13061.
9. Li, Q.; Guo, B. D.; Yu, J. G.; Ran, J. R.; Zhang, B. H.; Yan, H. J.; Gong, J. R. Highly Efficient Visible-Light-Driven Photocatalytic Hydrogen Production of CdS-Cluster-Decorated Graphene Nanosheets. *J. Am. Chem. Soc.* **2011**, *133*, 10878–10884.
10. Ng, Y. H.; Iwase, A.; Kudo, A.; Amal, R. Reducing Graphene Oxide on a Visible-Light $BiVO_4$ Photocatalyst for an Enhanced Photoelectrochemical Water Splitting. *J. Phys. Chem. Lett.* **2010**, *1*, 2607–2612.
11. Xiong, Z. G.; Zhang, L. L.; Zhao, X. S. Visible-Light-Induced Dye Degradation over Copper-Modified Reduced Graphene Oxide. *Chem.—Eur. J.* **2011**, *17*, 2428–2434.
12. Tu, W. G.; Zhou, Y.; Liu, Q.; Tian, Z. P.; Gao, J.; Chen, X. Y.; Zhang, H. T.; Liu, J. G.; Zou, Z. G. Robust Hollow Spheres Consisting of Alternating Titania Nanosheets and Graphene Nanosheets with High Photocatalytic Activity for

CO_2 Conversion into Renewable Fuels. *Adv. Funct. Mater.* **2012**, *22*, 1215–1221.
13. Kamat, P. V. Graphene-Based Nanoassemblies for Energy Conversion. *J. Phys. Chem. Lett.* **2011**, *2*, 242–251.
14. Lightcap, I. V.; Kosel, T. H.; Kamat, P. V. Anchoring Semiconductor and Metal Nanoparticles on a Two-Dimensional Catalyst Mat. Storing and Shuttling Electrons with Reduced Graphene Oxide. *Nano Lett.* **2010**, *10*, 577–583.
15. Bell, N. J.; Ng, Y. H.; Du, A. J.; Coster, H.; Smith, S. C.; Amal, R. Understanding the Enhancement in Photoelectrochemical Properties of Photocatalytically Prepared TiO_2-Reduced Graphene Oxide Composite. *J. Phys. Chem. C* **2011**, *115*, 6004–6009.
16. Du, J.; Lai, X. Y.; Yang, N. L.; Zhai, J.; Kisailus, D.; Su, F. B.; Wang, D.; Jiang, L. Hierarchically Ordered Macro-Mesoporous TiO_2-Graphene Composite Films: Improved Mass Transfer, Reduced Charge Recombination, and Their Enhanced Photocatalytic Activities. *ACS Nano* **2011**, *5*, 590–596.
17. Zhang, H.; Lv, X. J.; Li, Y. M.; Wang, Y.; Li, J. H. P25-Graphene Composite as a High Performance Photocatalyst. *ACS Nano* **2010**, *4*, 380–386.
18. Zhang, Y. H.; Tang, Z. R.; Fu, X. Z.; Xu, Y. J. TiO_2—Graphene Nanocomposites for Gas-Phase Photocatalytic Fegradation of Volatile Aromatic Pollutant: Is TiO_2—Graphene Truly Different From Other TiO_2—Carbon Composite Materials? *ACS Nano* **2010**, *4*, 7303–7314.
19. Yang, N. L.; Liu, Y. Y.; Wen, H.; Tang, Z. Y.; Zhao, H. J.; Li, L. Y.; Wang, D. Photocatalytic Properties of Graphdiyne and Graphene Modified TiO_2: From Theory to Experiment. *ACS Nano* **2013**, *7*, 1504–1512.
20. Zhuo, S. J.; Shao, M. W.; Lee, S. T. Upconversion and Downconversion Fluorescent Graphene Quantum Dots: Ultrasonic Preparation and Photocatalysis. *ACS Nano* **2012**, *6*, 1059–1064.
21. Gao, W.; Alemany, L. B.; Ci, L. J.; Ajayan, P. M. New Insights into the Structure and Reduction of Graphite Oxide. *Nat. Chem.* **2009**, *1*, 403–408.
22. Gómez-Navarro, C.; Weitz, R. T.; Bittner, A. M.; Scolari, M.; Mews, A.; Burghard, M.; Kern, K. Electronic Transport Properties of Individual Chemically Reduced Graphene Oxide Sheets. *Nano Lett.* **2007**, *7*, 3499–3503.
23. Mattevi, C.; Eda, G.; Agnoli, S.; Miller, S.; Mkhoyan, K. A.; Celik, O.; Mastrogiovanni, D.; Granozzi, G.; Garfunkel, E.; Chhowalla, M. Evolution of Electrical, Chemical, and Structural Properties of Transparent and Conducting Chemically Derived Graphene Thin Films. *Adv. Funct. Mater.* **2009**, *19*, 2577–2583.
24. Gan, Z. X.; Wu, X. L.; Zhou, G. X.; Shen, J. C.; Chu, P. K. Is There Real Upconversion Photoluminescence from Graphene Quantum Dots? *Adv. Opt. Mater.* **2013**, *1*, 554–558.
25. Huang, X. H.; El-Sayed, I. H.; Qian, W.; El-Sayed, M. A. Cancer Cell Imaging and Photothermal Therapy in The Near-Infrared Region by Using Gold Nanorods. *J. Am. Chem. Soc.* **2006**, *128*, 2115–2120.
26. Li, M.; Yang, X. J.; Ren, J. S.; Qu, K. G.; Qu, X. G. Using Graphene Oxide High Near-Infrared Absorbance for Photothermal Treatment of Alzheimer's Disease. *Adv. Mater.* **2012**, *24*, 1722–1728.
27. Robinson, J. T.; Tabakman, S. M.; Liang, Y. Y.; Wang, H. L.; Casalongue, H. S.; Vinh, D.; Dai, H. J. Ultrasmall Reduced Graphene Oxide with High Near-Infrared Absorbance for Photothermal Therapy. *J. Am. Chem. Soc.* **2011**, *133*, 6825–6831.
28. Yang, K.; Zhang, S.; Zhang, G. X.; Sun, X. M.; Lee, S. T.; Liu, Z. Graphene in Mice: Ultrahigh *in Vivo* Tumor Uptake and Efficient Photothermal Therapy. *Nano Lett.* **2010**, *10*, 3318–3323.
29. Hummers, W.; Offeman, R. E. Preparation of Graphitic Oxide. *J. Am. Chem. Soc.* **1958**, *80*, 1339.
30. Gan, Z. X.; Xiong, S. J.; Wu, X. L.; He, C. Y.; Shen, J. C.; Chu, P. K. Mn^{2+}-Bonded Reduced Graphene Oxide with Strong Radiative Recombination in Broad Visible Range Caused by Resonant Energy Transfer. *Nano Lett.* **2011**, *11*, 3951–3956.
31. Pan, J.; Liu, G.; Lu, G. Q.; Cheng, H. M. On the True Photoreactivity Order of {001}, {010}, and {101} Facets of Anatase TiO_2 Crystals. *Angew. Chem., Int. Ed.* **2011**, *50*, 2133–2137.
32. Ju, L.; Geng, B. S.; Horng, J.; Girit, C.; Martin, M.; Hao, Z.; Bechtel, H. A.; Liang, X. G.; Zettl, A.; Shen, Y. R.; *et al.* Graphene Plasmonics for Tunable Terahertz Metamaterials. *Nat. Nanotechnol.* **2011**, *6*, 630–634.
33. Koppens, F. H. L.; Chang, D. E.; de Abajo, F. J. G. Graphene Plasmonics: A Platform for Strong Light-Matter Interactions. *Nano Lett.* **2011**, *11*, 3370–3377.
34. Kaiser, A. B.; Gómez-Navarro, C.; Sundaram, R. S.; Burghard, M.; Kern, K. Electrical Conduction Mechanism in Chemically Derived Graphene Monolayers. *Nano Lett.* **2009**, *9*, 1787–1792.
35. Ruzicka, B. A.; Werake, L. K.; Zhao, H.; Wang, S.; Loh, K. P. Femtosecond Pump—Probe Studies of Reduced Graphene Oxide Thin Films. *Appl. Phys. Lett.* **2010**, *96*, 173106.
36. Kaniyankandy, S.; Achary, S. N.; Rawalekar, S.; Ghosh, H. N. Ultrafast Relaxation Dynamics in Graphene Oxide: Evidence of Electron Trapping. *J. Phys. Chem. C* **2011**, *115*, 19110–19116.
37. Lim, D. K.; Barhoumi, A.; Wylie, R. G.; Reznor, G.; Langer, R. S.; Kohane, D. S. Enhanced Photothermal Effect of Plasmonic Nanoparticles Coated with Reduced Graphene Oxide. *Nano Lett.* **2013**, *13*, 4075–4079.
38. Zedan, A. F.; Moussa, S.; Terner, J.; Atkinson, G.; El-Shall, M. S. Ultrasmall Gold Nanoparticles Anchored to Graphene and Enhanced Photothermal Effects by Laser Irradiation of Gold Nanostructures in Graphene Oxide Solutions. *ACS Nano* **2013**, *7*, 627–636.